



# Analysis of $k-\epsilon$ Budgets for Film Cooling Using Direct Numerical Simulation

Frank Muldoon\* and Sumanta Acharya†

Louisiana State University, Baton Rouge, Louisiana 70803

DOI: 10.2514/1.20597

Results of a direct numerical simulation of a film cooling jet are used to evaluate the terms in the standard  $k-\epsilon$  turbulence model. From the direct numerical simulation data all terms and correlations appearing in the exact  $k-\epsilon$  equations are reconstructed and compared with the models for these terms used in the standard  $k-\epsilon$  turbulence model. Unlike a channel flow, the turbulent diffusion terms that contain fluctuations of pressure are found to be significant and to have a different distribution from the turbulent diffusion terms involving only velocity fluctuations. Using an eddy viscosity derived from minimizing the error in representing the direct numerical simulation data by the Boussinesq gradient approximation, it is shown that the Boussinesq gradient approximation as used in the standard  $k-\epsilon$  turbulence model is a reasonable model for the various terms in the exact  $k-\epsilon$  equations. However, the expression for the eddy viscosity of the standard  $k-\epsilon$  turbulence model ( $C_\mu(k^2/\epsilon)Re$ ) is shown to be greatly in error. Using the direct numerical simulation data, two new damping functions are presented that greatly reduce the error in the eddy viscosity in the standard  $k-\epsilon$  turbulence model.

## Nomenclature

$f_\mu^{\text{dns}}$	= damping function defined by DNS
$k$	= $\frac{1}{2}u'_i u'_i$ , turbulent kinetic energy
$p$	= pressure
$Pr$	= Prandtl number
$Re$	= Reynolds number
$S_{i,j}$	= $\frac{1}{2}(\partial \bar{u}_i / \partial x_j + \partial \bar{u}_j / \partial x_i)$ , time-averaged strain rate tensor
$s$	= passive scalar
$U_0$	= maximum inlet crossflow velocity
$u$	= first component of velocity vector (i.e., $u_1$ )
$u_i$	= $i$ th component of velocity vector
$v$	= second component of velocity vector (i.e., $u_2$ )
$w$	= third component of velocity vector (i.e., $u_3$ )
$\epsilon$	= $-u'_{i,k} u'_{i,k}$
$1/Re_\tau$	= eddy viscosity

## I. Introduction

THE efficiency of turbine engines improves as the operating temperature of the working fluid in the turbine increases. Higher fluid temperatures in turbines leads to turbine blade failure as a result of exceeding temperature limits for the turbine blade material. A common means of cooling turbine blades is film cooling, where the goal is to protect the blade surface from the hot crossflow by a film of cooler fluid injected through holes in the blade surface. These film cooling holes must be designed in such a way that the coolant jet covers and remains near the blade surface and does not excessively penetrate into the crossflow. The film cooling jets consume a significant amount of process air and therefore an important design goal is to maximize the cooling and minimize the mass flow through the jets. For these reasons it is important to have accurate models for the flow and associated heat transfer when designing turbine blades.

The most commonly used turbulence model (the standard  $k-\epsilon$  model) is well known to have difficulty in film cooling applications. This model typically overpredicts the distance the jet penetrates into

the crossflow and underpredicts the jet spreading rate [1]. It is well known [2] to have difficulties in predicting flows with adverse pressure gradients as occurs in the recirculation region behind a film cooling jet. Despite these difficulties, the standard  $k-\epsilon$  model has been widely applied to film cooling flows as in [1,3,4]. Difficulties in predicting film cooling effectiveness at higher blowing ratios were reported by He et al. [4], and attributed to the failure of the turbulence model to correctly predict jet penetration. In a combined experimental and computational work, Ajersch et al. [3] found an overprediction of the streamwise and vertical velocity. They also reported significantly larger extrema for a Reynolds turbulent shear stress in the computations as compared to the experiments. An overprediction of the turbulent kinetic energy was seen in Hoda and Acharya [1]. An underprediction of lateral film cooling effectiveness (in comparison to experimental data) was found by Berhe and Patankar [5] and attributed to the underprediction of the lateral spreading of the jet. Greater jet penetration and a correspondingly reduced lateral spreading of the jet was found in Berhe and Patankar [6]. In a computational and experimental study, Harrington et al. [7] found a significant overprediction of jet penetration and a significant underprediction of jet lateral spreading. Using the standard  $k-\epsilon$  model Radomsky and Thole [8] found a large overprediction of the turbulent kinetic energy and one of the Reynolds turbulent shear stresses for flow in a turbine vane passage. In a series of papers on film cooling flows, Medic and Durbin [9,10] obtained significant improvements in prediction of turbulent kinetic energy and heat transfer coefficients by the use of limiters in the standard  $k-\epsilon$  model.

There are very few studies in the literature concerning direct numerical simulation (DNS) or large eddy simulation (LES) of film cooling flows. An unsteady simulation of a circular jet in crossflow was performed by Hahn and Choi [11] on a  $705 \times 161 \times 129$  grid using second-order central difference schemes. The Reynolds number was 1750 and the blowing ratio was 0.5. The delivery tube was not modeled in their work, which solved the incompressible Navier-Stokes equations but not the energy equation. Muldoon and Acharya [12] used higher-order finite difference schemes in an unsteady simulation to study a normally injected film cooling jet which included the flow development in the delivery tube. This work presented the unsteady interactions of the upstream crossflow and horseshoe vortex system with flow development in the delivery tube, and showed that this unsteady interaction resulted in a periodic pulsing of the jet at a Strouhal number of 0.44. An LES of a film cooling jet was done in a series of papers [13–15] which investigated the influence of various parameters on the flow physics of square or rectangular coolant jets issuing normally into the crossflow, similar

Received 8 December 2005; revision received 18 April 2006; accepted for publication 2 May 2006. Copyright © 2006 by the American Institute of Aeronautics and Astronautics, Inc. All rights reserved. Copies of this paper may be made for personal or internal use, on condition that the copier pay the \$10.00 per-copy fee to the Copyright Clearance Center, Inc., 222 Rosewood Drive, Danvers, MA 01923; include the code \$10.00 in correspondence with the CCC.

\*Center for Computation and Technology

†Department of Mechanical Engineering

to the experimental setup of Ajersch et al. [3]. Whereas the reported DNS/LES studies have shown improvements in predictive capabilities vs Reynolds-averaged Navier-Stokes studies, due to the computational expense of DNS/LES, Reynolds-averaged Navier-Stokes methods are the predominant industrial design tool for film cooling flows. Therefore, it is important to improve the turbulence models used in Reynolds-averaged Navier-Stokes solutions to improve their predictive capabilities for film cooling flows.

Using DNS data, the terms in the  $k-\varepsilon$  equations have been examined for a channel flow problem in which mean gradients exist only in one dimension [16]. These one-dimensional data have been examined and used to improve the  $k-\varepsilon$  turbulence model [17]. However, for the three-dimensional film cooling configuration of interest here, the authors are not aware of previous work where the  $k-\varepsilon$  equations were examined with the aid of DNS, and model improvements proposed.

The purpose of the present work is to show how the terms in the commonly used standard  $k-\varepsilon$  model behave for the basic jet-in-crossflow configuration with jet parameters representative of film cooling. This is done by computing (using DNS) the terms in the exact  $k$  and  $\varepsilon$  equations and the standard  $k-\varepsilon$  model. The modeled terms are then compared with the terms they model in the exact  $k$  and  $\varepsilon$  equations. This comparison shows what parts of the exact  $k$  and  $\varepsilon$  equations are significant, along with how well the standard models for the various terms perform for this type of flow. This study should provide guidance for turbulence modelers in developing turbulence models that are designed for film cooling jets in crossflow. In addition, a new wall damping function for the eddy viscosity suitable for film cooling flows is presented.

It should be noted that for flows in which DNS data have been used to analyze the terms in the exact  $k-\varepsilon$  equations, such as a fully developed channel flow in which mean gradients exist in only one dimension, presentation of the results is greatly simplified as all terms are one-dimensional. For the flow examined in the present work, mean gradients exist in all three dimensions which greatly complicates the analysis and presentation of the terms in the  $k-\varepsilon$  equations. The use of line plots, although offering a direct quantitative comparison, can be misleading as they only offer a view in one dimension from a specific point in the other two dimensions of a flow which changes greatly in all three dimensions. To clearly present the three-dimensional aspect of the flow, the authors have made extensive use of three-dimensional contour plots. Whereas this makes more difficult quantitative comparisons, it greatly aids the comparison of three-dimensional distributions.

## II. Governing Equations and Discretization

In the present work, the nonconservative form of the unsteady incompressible three-dimensional Navier-Stokes equations [Eqs. (1) and (2)] is used to model the flow, along with an equation describing the evolution of a passive scalar [Eq. (3)].

$$\frac{\partial u_i}{\partial x_i} = 0 \quad (1)$$

$$\frac{\partial u_i}{\partial t} + u_j \frac{\partial u_i}{\partial x_j} = -\frac{\partial p}{\partial x_i} + \frac{1}{Re} \frac{\partial^2 u_i}{\partial x_j \partial x_j} \quad (2)$$

$$\frac{\partial s}{\partial t} + u_j \frac{\partial s}{\partial x_j} = \frac{1}{Re Pr} \frac{\partial^2 s}{\partial x_j \partial x_j} \quad (3)$$

Equations (1–3), are solved in nondimensional form, in which the properties of the fluid and the passive scalar are described by the Reynolds number and the Prandtl number. These equations are solved without the use of a model for turbulence, i.e., a DNS is performed. Solutions are obtained on parallel computer systems using the computer program Tetra [18] which has been written using Fortran 95 and MPI for use on high performance parallel computers.

Calculations are done on a staggered mesh where the discrete pressure and passive scalar are located at the main grid points and the velocity components are staggered in their respective directions. A sixth-order central difference convective scheme with a monotonic limiter is used along with fourth-order interpolation for the velocity in the convective terms, e.g., for  $v$  in  $v(\partial u / \partial y)$ , etc. A fourth-order central difference scheme is used for the diffusive terms. The pressure gradient and the continuity equation are represented by second-order centered schemes. A third-order accurate explicit time integration scheme is used to integrate the convective and diffusive terms in time; the pressure gradient is treated fully implicitly. The equation for the transport of the passive scalar is represented using the same order and type of schemes used for the momentum equations. Equations (1) and (2) are solved using the colored symmetric coupled Gauss Seidel (SCGS) method. The accuracy of all finite difference stencils is maintained near nonperiodic boundaries by shifting toward the boundary the point at which the stencil is evaluated. Further details of the finite difference schemes and the computer code used in the present work can be found in Muldoon [18].

## III. Turbulence Modeling

Any unsteady quantity  $u(t)$  can be decomposed into the following two parts,  $u(t) = u'(t) + \bar{u}$ , where  $\bar{u}$  indicates the time-averaged or mean part and  $u'(t)$  the fluctuating part. Throughout this paper the prime ( $u'$ ) indicates fluctuating quantities whereas the overbar ( $\bar{u}$ ) indicates time-averaged quantities. The Reynolds-averaged Navier-Stokes equations [Eqs. (4) and (5)] are obtained by time averaging the Navier-Stokes equations [Eqs. (1) and (2)].

$$\frac{\partial \bar{u}_i}{\partial x_i} = 0 \quad (4)$$

$$\bar{u}_j \frac{\partial (\bar{u}_i)}{\partial x_j} + \frac{\partial (\bar{u}'_i \bar{u}'_j)}{\partial x_j} = -\frac{\partial \bar{p}}{\partial x_i} + \frac{1}{Re} \frac{\partial^2 \bar{u}_i}{\partial x_j \partial x_j} \quad (5)$$

The goal of turbulence modeling is to derive an expression for  $\overline{u'_i u'_j}$  and  $\overline{u'_i s'}$ . The Boussinesq gradient approximation Eq. (6), which requires a definition for the eddy viscosity, is used in the standard  $k-\varepsilon$  model and most other two-equation turbulence models to represent the turbulent Reynolds stresses ( $\overline{u'_i u'_j}$ ) which appear in the Reynolds-averaged Navier-Stokes equations [Eqs. (4) and (5)].

$$-\overline{u'_i u'_j} = \frac{1}{Re_\tau} 2S_{i,j} - \frac{2}{3} k \delta_{i,j} \quad (6)$$

In the standard  $k-\varepsilon$  model, the eddy viscosity is defined as  $C_\mu (k^2 / \varepsilon) Re$ . Equations for  $k$  and  $\varepsilon$  can be derived without any assumptions or simplifications from the Navier-Stokes equations, details of which can be found in [2]. As a result of the nonlinearity of the Navier-Stokes equations, these equations for  $k$  and  $\varepsilon$  contain numerous high-order correlations, which must be modeled. The present work compares the exact equations for  $k$  and  $\varepsilon$  in which these correlations are determined using DNS with the model for these correlations given by the standard  $k-\varepsilon$  model of Launder and Spalding [19]. When comparing the model for the correlations with the correlations obtained from DNS, all quantities in the model (i.e.,  $k$ ,  $\varepsilon$ , and  $\bar{u}_i$ ) are obtained from the same DNS. This allows a direct evaluation of the quality of the model. The DNS is used as a numerical experiment as it is extremely difficult or impossible to obtain some of the complicated correlations in the  $k-\varepsilon$  equations from experimental measurements; therefore this is the only feasible method with which these correlations can be obtained.

### A. $k-\varepsilon$ Equations

#### 1. Exact and Modeled Equations for $k$

The exact  $k$  equation is given by Eq. (7). Note that Eqs. (7) and (9) use the comma notation to indicate differentiation (i.e.,  $u_{k,m} =$

$\partial u_k / \partial x_m$  and  $u'_{i,km} = \partial u'_i / \partial x_k \partial x_m$ .

$$\frac{\partial k}{\partial t} + \bar{u}_j \frac{\partial k}{\partial x_j} = -\overline{u'_i u'_j} \frac{\partial \bar{u}_i}{\partial x_j} - \frac{1}{Re} \varepsilon + \frac{\partial}{\partial x_j} \left[ \frac{1}{Re} \frac{\partial k}{\partial x_j} - \frac{1}{2} \overline{u'_i u'_i u'_j} - \overline{p' u'_j} \right] \quad (7)$$

The modeled  $k$  equation is given by Eq. (8) [19].

$$\frac{\partial k}{\partial t} + \bar{u}_j \frac{\partial k}{\partial x_j} = 2C_\mu \frac{k^2}{\varepsilon} S_{i,j} S_{i,j} Re - \frac{1}{Re} \varepsilon + \frac{\partial}{\partial x_j} \left[ \frac{1}{Re} \frac{\partial k}{\partial x_j} + \frac{C_\mu (k^2/\varepsilon)}{\sigma_k} \frac{\partial k}{\partial x_j} Re \right] \quad (8)$$

The values of the various constants appearing in Eq. (8) are

$$C_\mu = 0.09 \quad \sigma_k = 1$$

The terms of Eqs. (7) and (8) are commonly referred to by the following names, which reflect their predominant effect on  $k$  (the terms that are modeled are indicated):

Convective transport of  $k = \partial k / \partial t + \bar{u}_j (\partial k / \partial x_j)$   
Production of  $k = 2C_\mu (k^2/\varepsilon) S_{i,j} S_{i,j} Re$  [model of  $-\overline{u'_i u'_j} (\partial \bar{u}_i / \partial x_j)$ ]  
Dissipation of  $k = -(1/Re) \varepsilon$   
Molecular diffusion of  $k = (\partial / \partial x_j) [(1/Re) (\partial k / \partial x_j)]$   
Turbulent diffusion of  $k = (\partial / \partial x_j) \{ [C_\mu (k^2/\varepsilon) / \sigma_k] (\partial k / \partial x_j) Re \}$   
[model of  $(\partial / \partial x_j) (-\frac{1}{2} \overline{u'_i u'_i u'_j} - \overline{p' u'_j})$ ]

## 2. Exact and Modeled Equations for $\varepsilon$

The exact  $\varepsilon$  equation is given by Eq. (9).

$$\frac{\partial \varepsilon}{\partial t} + \bar{u}_j \frac{\partial \varepsilon}{\partial x_j} = -2[\overline{u'_{i,k} u'_{j,k}} + \overline{u'_{k,i} u'_{k,j}}] \frac{\partial \bar{u}_i}{\partial x_j} - 2\overline{u'_k u'_{i,j}} \frac{\partial^2 \bar{u}_i}{\partial x_k \partial x_j} - 2\overline{u'_{i,k} u'_{i,m} u'_{k,m}} - 2\overline{u'_{i,km} u'_{i,km}} \frac{1}{Re} + \frac{\partial}{\partial x_j} \left[ \frac{\partial \varepsilon}{\partial x_j} \frac{1}{Re} - \overline{u'_j u'_{i,m} u'_{i,m}} - 2\overline{p'_{i,m} u'_{j,m}} \right] \quad (9)$$

The modeled  $\varepsilon$  equation is given by Eq. (11) [19].

$$\frac{\partial \varepsilon}{\partial t} + \bar{u}_j \frac{\partial \varepsilon}{\partial x_j} = 2C_{\varepsilon 1} C_\mu k S_{i,j} S_{i,j} Re - C_{\varepsilon 2} \frac{\varepsilon^2}{k Re} + \frac{\partial}{\partial x_j} \left[ \frac{1}{Re} \frac{\partial \varepsilon}{\partial x_j} + \frac{C_\mu Re k^2}{\sigma_\varepsilon} \frac{\partial \varepsilon}{\partial x_j} \right] \quad (10)$$

The values of the various constants appearing in Eq. (10) are

$$C_{\varepsilon 1} = 1.44 \quad C_{\varepsilon 2} = 1.92 \quad C_\mu = 0.09 \quad \sigma_\varepsilon = 1.3$$

The terms of Eqs. (9) and (10) are commonly referred to by the following names, which reflect their predominant effect on  $\varepsilon$  (the terms that are modeled are indicated):

Convective transport of  $\varepsilon = \partial \varepsilon / \partial t + \bar{u}_j (\partial \varepsilon / \partial x_j)$   
Production of  $\varepsilon = 2C_{\varepsilon 1} C_\mu k S_{i,j} S_{i,j} Re$  [models  $-2(\overline{u'_{i,k} u'_{j,k}} + \overline{u'_{k,i} u'_{k,j}})(\partial \bar{u}_i / \partial x_j) - 2\overline{u'_k u'_{i,j}} (\partial^2 \bar{u}_i / \partial x_k \partial x_j)]$   
Destruction of  $\varepsilon = -C_{\varepsilon 2} (\varepsilon^2 / k Re)$  [models  $-2\overline{u'_{i,k} u'_{i,m} u'_{k,m}} - 2\overline{u'_{i,km} u'_{i,km}} (1/Re)$ ]  
Molecular diffusion of  $\varepsilon = (\partial / \partial x_j) [(\partial \varepsilon / \partial x_j) (1/Re)]$   
Turbulent diffusion of  $\varepsilon = (\partial / \partial x_j) [(C_\mu Re / \sigma_\varepsilon) (k^2 / \varepsilon) (\partial \varepsilon / \partial x_j)]$   
[model of  $(\partial / \partial x_j) (-\overline{u'_i u'_{i,m} u'_{i,m}} - 2\overline{p'_{i,m} u'_{j,m}})]$

The terms in Eq. (7) and particularly Eq. (9) are extremely complicated with some containing mixed derivatives. As Eqs. (1) and (2) are solved on a staggered grid on which all three velocity components are defined on different grids from each other and from the main grid where pressure and the scalar are defined, it is necessary to specify a grid on which to evaluate Eqs. (7) and (9). Because the

main grid is chosen for the grid on which Eqs. (7) and (9) are evaluated, this requires that the velocities be interpolated from their respective grids onto the main grid. Once this is done the terms in Eqs. (7) and (9) may be computed. The interpolation and differentiation operators used for the terms in Eqs. (7) and (9) are sixth-order accurate. They are derived independently of the operators used in discretizing Eqs. (1–3). As Eqs. (7) and (9) are derived from Eqs. (1) and (2) and then discretized on a different grid with operators different from those used in Eqs. (1) and (2), the residual of Eqs. (7) and (9) relative to the terms of Eqs. (7) and (9) will likely not be of the same order as the residual of Eqs. (1) and (2) is relative to the terms of Eqs. (1) and (2). The alternative would be to derive discretized versions of Eqs. (7) and (9) directly from the discretized versions of Eqs. (1) and (2). This would ensure that the residuals of Eqs. (7) and (9) will be of the same order relative to the terms in the equations as is the case for Eqs. (1) and (2); however, this is impractical due to the complexity of the correlations and the high-order discretization stencils used to discretize Eqs. (1) and (2). Details concerning the discretization of the exact  $k$  and  $\varepsilon$  equations on inflow boundaries can be found in Muldoon [18].

## IV. Eddy Viscosity

As the eddy viscosity appears frequently in numerous terms in two-equation turbulence models including the standard  $k-\varepsilon$  model, it is examined in detail in the present work. The eddy viscosity can be computed from Eq. (6) using the results of a DNS to calculate  $\overline{u'_i u'_j}$ ,  $S_{i,j}$ , and  $k$ . It is desired to obtain the value for  $1/Re_\tau$  from Eq. (6), which will minimize the error in representing  $\overline{u'_i u'_j}$  by the right-hand side of Eq. (6). This is done by minimizing the square of the error with respect to  $1/Re_\tau$ . Advantage is not taken of the symmetry of  $\overline{u'_i u'_j}$  in defining the error in Eq. (6). The rationale for this is that in the Reynolds-averaged Navier-Stokes equations, the off-diagonal terms appear twice as often as the diagonal. Therefore it is natural to preserve this ratio in minimizing the error associated with representing  $\overline{u'_i u'_j}$  by the Boussinesq gradient approximation [Eq. (6)].

$$\text{error} = \sum_{j=1}^3 \sum_{i=1}^3 \left( \frac{1}{Re_\tau} 2S_{i,j} - \frac{2}{3} k \delta_{i,j} + \overline{u'_i u'_j} \right)^2$$

$$\frac{\partial(\text{error})}{\partial(1/Re_\tau)} = 0 = \sum_{j=1}^3 \sum_{i=i}^3 2 \left( \frac{1}{Re_\tau} 2S_{i,j} - \frac{2}{3} k \delta_{i,j} + \overline{u'_i u'_j} \right) 2S_{i,j}$$

which results in:

$$\frac{1}{Re_\tau} = \frac{\sum_{j=1}^3 \sum_{i=1}^3 (\frac{2}{3} k \delta_{i,j} S_{i,j} - \overline{u'_i u'_j} S_{i,j})}{\sum_{j=1}^3 \sum_{i=1}^3 2S_{i,j} S_{i,j}} \quad (11)$$

Note that as the expression for the error is a quadratic polynomial in  $1/Re_\tau$ , there is a guaranteed global minimum which occurs at the value of  $1/Re_\tau$  given by Eq. (11). It should be noted that this approach for minimizing the error is different from the traditional approaches adopted so far where, due to the one nonhomogeneous dimension in the idealized problems considered, only one component of  $\overline{u'_i u'_j}$  and  $S_{i,j}$  is important. For more complex three-dimensional flows with no homogeneous dimensions, the aforementioned minimization process appears to be the most logical approach for computing  $1/Re_\tau$ .

## V. Problem Description

The modeled flow is similar to that of Kaszeta [20]. In this experimental work, an inclined jet with a delivery tube and plenum was examined. As the goal is to obtain DNS data for a representative film cooling geometry, we decided not to model the plenum and delivery tube in the DNS. This decision is a result of the stringent spatial and temporal resolution requirements of DNS. It has been

decided that it is better to use the available resolution in the region of most interest (over the blade surface) where accurate data are needed for use in improving turbulence models. The inclusion of the plenum and delivery tube will undoubtedly result in changes, but these changes are not expected to result in differences in the important physics of the flow. However, to model the effect of the delivery tube and plenum as closely as possible, the boundary condition at the jet exit is specified as the mean velocity obtained from a simulation that includes a plenum and delivery tube. Thus a preliminary simulation is done including the plenum and delivery tube with a jet inclination angle of 35 deg from the crossflow. From this simulation a mean jet exit velocity boundary condition is extracted and used in a second set of simulations in which all grid points are in the jet-crossflow region. All results presented in this work are computed from this second set of simulations.

A schematic of the flow domain along with boundary conditions and dimensions is given in Fig. 1. The origin of the coordinate system is defined to be the center of the jet at the blade surface. In Fig. 1  $L_{\text{up}} = 3.6d$ ,  $L_{\text{down}} = 14d$ ,  $L_{\text{freestream}} = 4.5d$ ,  $L_z = 3d$ . All quantities are nondimensionalized by the jet diameter  $d$  and the maximum inlet crossflow velocity  $U_0$ . At the crossflow inlet boundary at  $x = L_{\text{up}}$ , the  $v$ - and  $w$ -components of velocity are set to zero whereas the following profile is used for the  $u$ -velocity.

$$u(y) = \begin{cases} U_0 \left(\frac{y}{2}\right)^{1/7} & 0 \leq y \leq 2 \\ U_0 & y > 2 \end{cases}$$

At the jet exit, the time-averaged results obtained from the simulation including the plenum and delivery tube are used as the boundary condition for all three components of the velocity. This time-averaged velocity should be symmetric about the  $z$ -axis. However, due to the finite time-averaging period, the profile is not exactly symmetric. Symmetry is therefore enforced by averaging the profile around the  $z$ -axis. The Reynolds number based on the average velocity through the jet ( $U_{\text{jet}}$ ) and jet diameter is 3068; the Prandtl number is 0.707. The average blowing ratio, defined as the ratio  $U_{\text{jet}}/U_0$  is 0.24 whereas the blowing ratio based on the maximum jet exit velocity is 0.53. The passive scalar is set to zero at  $y = 0$  within the jet exit; if outside the jet exit at  $y = 0$  the gradient of the passive scalar is set to zero. No-slip boundary conditions are applied at  $y = 0$  outside of the jet exit. A symmetry boundary condition is applied at  $y = L_{\text{freestream}}$ , a convective boundary condition at  $x = L_{\text{down}}$ , and a periodic boundary condition in the  $z$ -direction.

Three grids, with dimensions of  $286 \times 80 \times 70$ ,  $574 \times 161 \times 142$ , and  $1150 \times 323 \times 286$  are used. The grids are obtained by doubling the number of points in each dimension of the next coarsest grid, while keeping the grid stretching parameters the same. The time steps used on the grids are 0.008, 0.004, and 0.002, respectively. This results in maximum CFL numbers of  $\sim 0.2$  in the  $x$ -direction,  $\sim 0.1$  in the  $y$ -direction, and  $\sim 0.08$  in the  $z$ -direction. The results shown in the present work are obtained on the  $1150 \times 323 \times 286$  grid, with the other grids being used to verify grid independence.

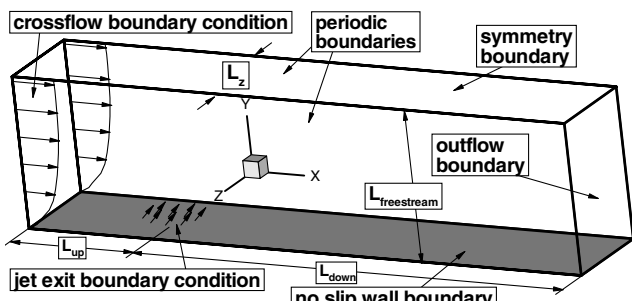


Fig. 1 Inclined jet in crossflow with prescribed exit conditions 3-D schematic.

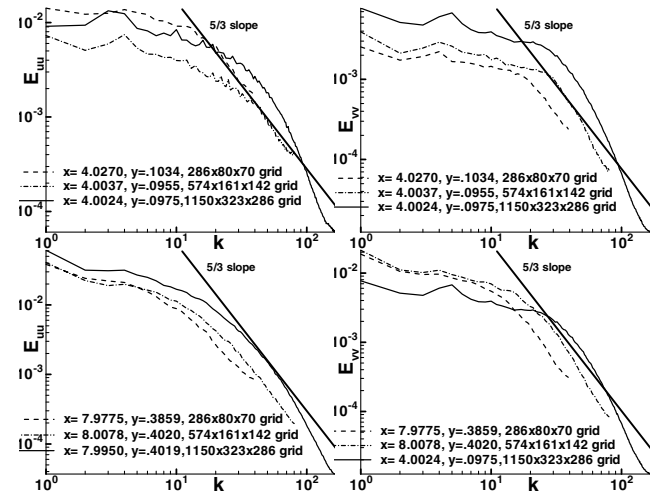


Fig. 2 One-dimensional spatial energy spectrum in  $z$ -direction.

## VI. Validation

### A. Energy Spectra

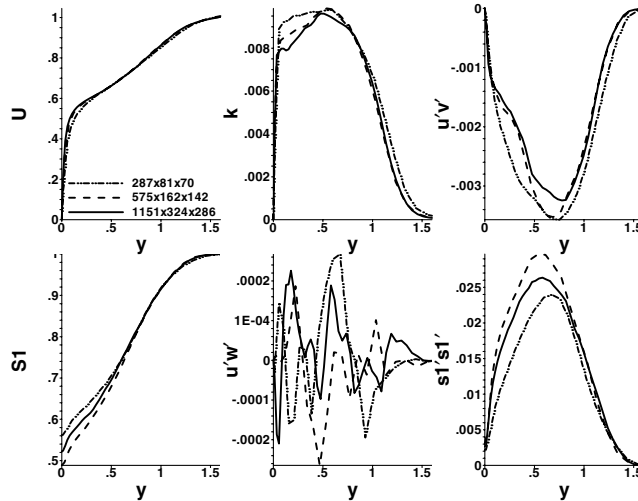
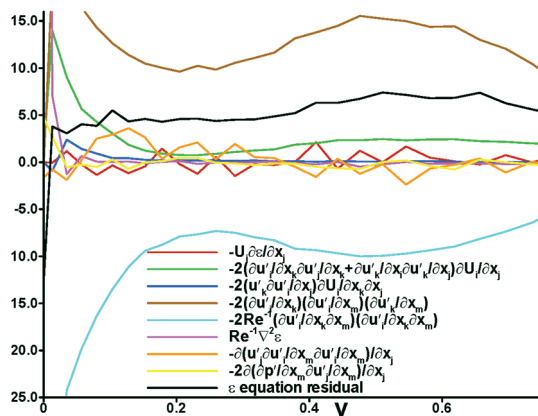
Figure 2 shows one-dimensional spatial energy spectra in the  $z$ -direction of the  $x$ - and  $y$ -components of velocity. This spectra is obtained by interpolating the velocity on the uneven spatial grid onto an even grid which is defined by the smallest grid spacing in the uneven grid and then transforming into discrete wave number space. Regions in which the slope of the spectra matches the  $5/3$  slope predicted by the turbulence theory of Kolmogoroff [21] can be seen. Close agreement can be seen between the results obtained on the  $574 \times 161 \times 142$  grid and on the  $1150 \times 323 \times 286$  grid. The good agreement with the results from the coarser grids may be due to the use of a monotonic convection scheme, which adds viscosity in regions where the gradients are large to prevent overshoots and undershoots. As a result, on an unresolved grid, the scheme behaves as a LES model in which the model for the unresolved scales is the added viscosity. This effect has been termed monotonic-integrated large eddy simulation (MILES) by Oran and Boris [22].

### B. Convergence of Statistics

In the present work all statistics are computed as a running average. The numerous terms that must be computed as a running average to reconstitute the correlations appearing in the exact  $k$  and  $\varepsilon$  equations [Eqs. (7) and (9)] are given in Muldoon [18]. Statistics are averaged over 567,822 time steps on the  $1150 \times 323 \times 286$  grid after an initialization period of 64,000 time steps to allow the flow to become statistically fully developed and eliminate the effect of the initial conditions. The sampling rate is one, i.e., the solution at every time step is used in determining the statistics. With a time step of 0.002, this corresponds to the flow traveling  $1136d$  and  $128d$  at  $U_0$ , respectively. These time-averaging periods are met or exceeded on the coarser grids.

Figure 3 shows statistics on the three grids; the small difference between the two finest grids is evidence of essentially grid independent results. Note that for this geometry and boundary conditions, in particular, the time invariance of the boundary conditions, the Reynolds stress  $\bar{u}'w'$  is theoretically zero at the jet centerline (Muldoon [18]) and its value serves as an indicator of the quality of the time-averaging period and sampling rate. As it is an order of magnitude less than the other (nonzero) Reynolds stress components this suggests that the time-averaging period and sampling rate are sufficient.

Because Eqs. (7) and (9) are not derived from discretized versions of Eqs. (1) and (2), the residuals of Eqs. (7) and (9) are not expected to be of the same order relative to the terms in Eqs. (7) and (9) as the residuals of Eqs. (1) and (2) are relative to the terms in Eqs. (1) and (2). However, the residuals of Eqs. (7) and (9) should decrease with the order of spatial accuracy of the method used to compute them if

Fig. 3 Statistics on different grids,  $x = 13d$ ,  $z = 0$ .Fig. 4 All terms in the exact  $\epsilon$  equation [Eq. (9)] at  $x = 8d$ ,  $z = 0$ .

the temporal averaging period and sampling rate is sufficient. Assuming that the residual is dominated by the lowest order truncation error terms, the order of convergence in the residual as the grid spacing is reduced can be computed. Using the  $L_\infty$  norm of the residual the order of convergence in the residual of Eq. (7) is found to be 1.45 using the  $286 \times 80 \times 70$  and  $574 \times 161 \times 142$  grids and 2.43 using the  $574 \times 161 \times 142$  and  $1150 \times 323 \times 286$  grids. As the overall order of convergence of the numerical method is given by the lowest order schemes used, which is second-order for both the continuity equation and the pressure gradient; this shows that this order of convergence is maintained in computing the terms in the  $k$  equation. Using this same norm, the order of convergence in the residual of Eq. (9) is 0.38 and 0.17, respectively. It is known to be difficult to compute a balanced  $\epsilon$  equation [23]; this is likely due to the large number of extremely complicated terms involving high-order correlations in this equation. Nevertheless, the residual, whereas not decaying at the rate expected from the spatial accuracy of the numerical scheme, is bounded by other terms in Eq. (7). Figure 4 shows the residual to be bounded by  $-2\bar{u}'_{i,k} \bar{u}'_{i,m} \bar{u}'_{k,m}$  (one of the terms comprising the production of  $\epsilon$ ) and  $-2\bar{u}'_{i,km} \bar{u}'_{i,km} (1/Re)$  (one of the terms comprising the destruction of  $\epsilon$ ).

## VII. Flow Physics

Jets in crossflow contain a number of distinct flow structures [24]. These structures are a counterrotating vortex pair (CVP) of kidney-shaped vortices, a horseshoe vortex, shear layer vortices, and upright wake vortices. As the jet is deflected by the crossflow it splits into the CVP. Whereas it is difficult to distinguish the CVP in an instantaneous image of the flowfield (Fig. 5), it can be clearly seen if

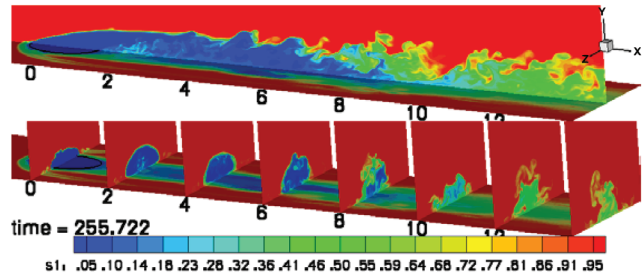


Fig. 5 Instantaneous contours of scalar.

the time-averaged flowfield is examined, as discussed later (Fig. 7). The CVP entrains fluid from the crossflow into the jet, promoting mixing of the jet with the crossflow. As a result of vortex induction, the CVP causes the jet to lift away from the surface, which is undesirable for film cooling. The horseshoe vortex forms upstream of the jet, wraps around the jet, and reorients itself in the streamwise direction (Fig. 5). This vortex is actually a number of vortices (see Fig. 7) and remains close to the blade surface. Its role is to entrain coolant fluid from the jet and thereby cool the blade surface along its trajectory as seen in Fig. 5. Shear layer vortices form at the boundary between the jet and the crossflow (Fig. 5). These vortices begin small but grow into large scale structures by  $3d$ – $4d$  downstream of the jet center. Behind the jet a region of low pressure and velocity is formed. In this region a recirculation pattern emerges that entrains fluid into the jet. Wake vortices are not seen in this flow, likely due to the low blowing ratio and small jet inclination angle which result in a jet close to the blade surface.

## VIII. Budgets

### A. First- and Second-Order Statistics

The mean scalar is shown in various planes in Fig. 6c. Note that the maximum and minimum shown on figures in this work apply to the surfaces shown in the figures and not the entire field. The signature of the horseshoe vortex on the blade surface shows up distinctly in this figure. The horseshoe vortex entrains a small amount of fluid from the leading edge of the jet, and transports it downstream as the vortex wraps around the jet and orients itself in the streamwise direction. The effect of the horseshoe vortex in keeping the velocity magnitude small near the blade surface is evident in Fig. 6b, which shows a crossflow region between the horseshoe vortex and the CVP near the

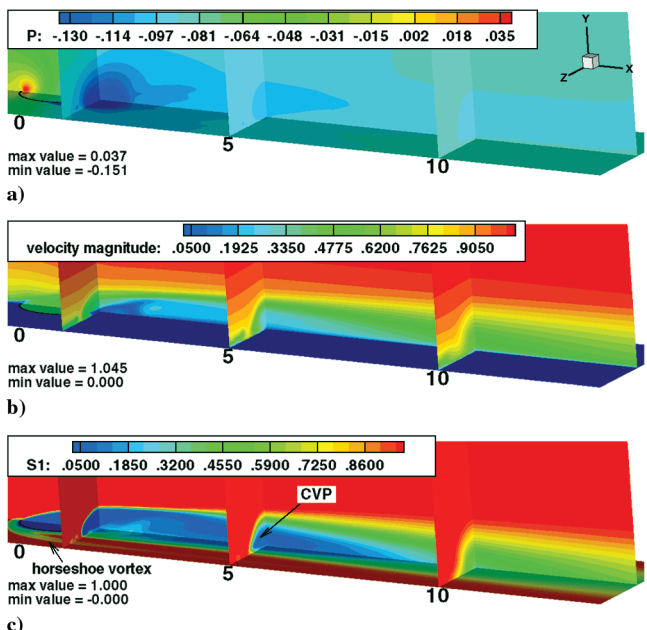


Fig. 6 Three-dimensional view of time-averaged pressure, velocity magnitude, and scalar.

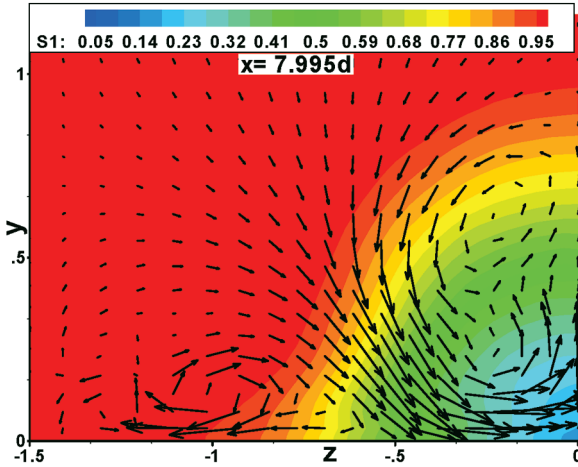


Fig. 7 Time-averaged velocity vectors and contours of scalar field in  $y-z$  plane at  $x \approx 8d$ .

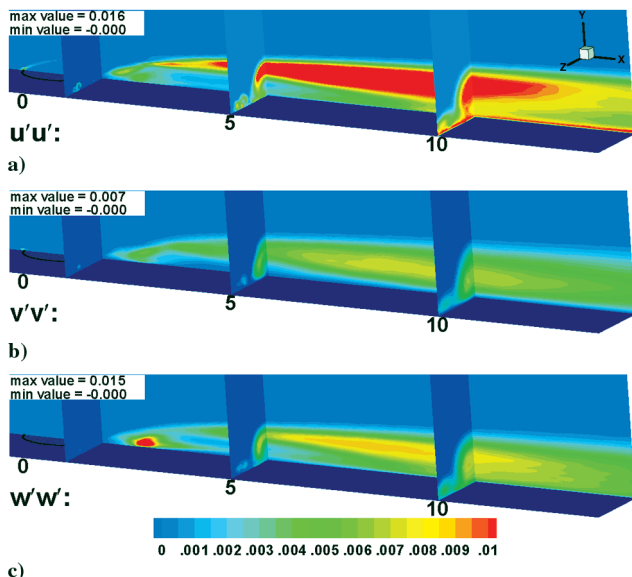


Fig. 8 Three-dimensional view of  $\overline{u'v'}$ ,  $\overline{v'v'}$ ,  $\overline{w'w'}$ .

blade surface in which the velocity magnitude is large. A stagnation region in front of the jet, where the horseshoe vortex forms, and a low-pressure region behind the jet can be seen in the mean pressure field in Fig. 6a. A region behind the jet at  $x \approx 2d$ , in which the value of the scalar on the blade surface is higher than further downstream, can be seen in Fig. 6c. This likely is a result of the recirculation pattern in this region in which crossflow fluid is entrained into the jet wake. The CVP and the horseshoe vortex can be seen in Fig. 7, in which for clarity every eighth vector in each direction and half of the domain in the (symmetric)  $z$ -direction is shown. The horseshoe vortex consists of two vortices with opposite rotation, whereas the CVP is seen to form two vortices with the same sense of rotation.

The normal Reynolds stresses are shown in Fig. 8. The  $\overline{u'u'}$  component is larger than the other components and has its highest values in the shear layer where large velocity gradients exist. The  $\overline{u'u'}$  component also dominates the horseshoe vortex, growing significantly in strength as the horseshoe vortex convects in the downstream direction. It starts to form a peak near the wall at  $x \approx 10d$ . The smallest component is  $\overline{v'v'}$ , which spreads towards the wall as the downstream distance increases. A spike in the  $\overline{w'w'}$  component exists in the recirculation region behind the jet at  $x \approx 2d$  where the crossflow collides in the  $z$ -direction after wrapping around the jet.

The shear stress components of the Reynolds stress tensor are shown in Fig. 9. The strong anisotropy of the flow field can be seen in

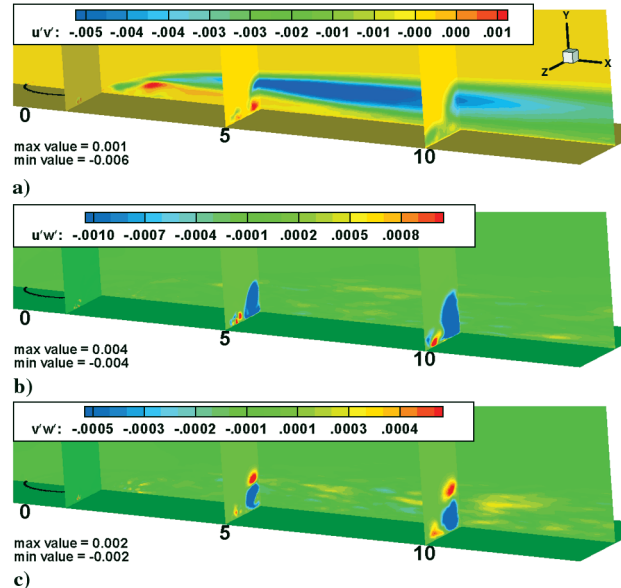


Fig. 9 Three-dimensional view of  $\overline{u'v'}$ ,  $\overline{v'w'}$ ,  $\overline{v'w'}$ .

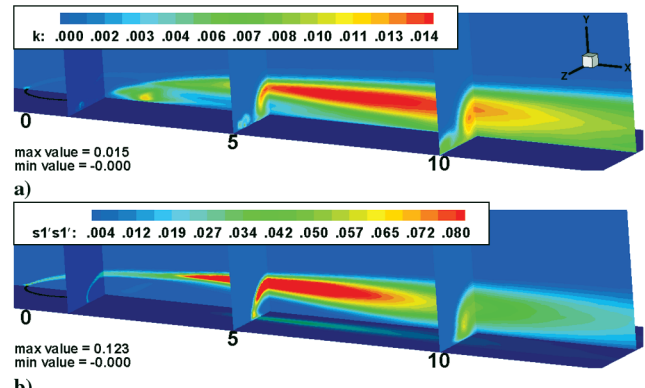


Fig. 10 Three-dimensional view of  $k$ ,  $\overline{s's'}$ .

this figure. In particular the  $\overline{v'w'}$  component experiences a sign change that occurs near the boundary between the jet and the crossflow and appears clearly in the  $y-z$  plane at  $x \approx 5d$  in Fig. 9c.

Figure 10 shows that the scalar fluctuations are highest in the shear layer and reach a maximum at  $x \approx 5d$ . The scalar fluctuations are small in the horseshoe vortex. The turbulent kinetic energy has a different behavior, reaching a maximum further downstream at roughly  $x \approx 7.5d$  and is significant in the horseshoe vortex. It can be seen that turbulent kinetic energy in the recirculation region is small except for a peak at  $x \approx 2d$ , which is due to the contribution of  $\overline{w'w'}$ .

## B. Eddy Viscosity

Overprediction of the eddy viscosity by the model  $[C_\mu(k^2/\varepsilon)Re]$  can be seen quite clearly in Fig. 11c. The eddy viscosity obtained from DNS [using Eq. (11)] is actually negative in certain regions, which is not permitted by the model  $[C_\mu(k^2/\varepsilon)Re]$ , in which the eddy viscosity is always positive. The eddy viscosity obtained from Eq. (11) enables some modeled terms (as discussed later) to be represented accurately, a factor which perhaps should be considered in the design of turbulence models, which traditionally assume that the eddy viscosity is positive. It can be clearly seen that the modeled eddy viscosity overpredicts the values obtained from the DNS and Eq. (11). Therefore calculations done with the traditional eddy viscosity expression are likely to overpredict jet spreading and turbulence levels. Using the wall normal turbulent fluctuations in the expression for the eddy viscosity  $[C_\mu \frac{3}{2}(\overline{v'v'}k/\varepsilon)Re]$  can be seen (Fig. 11b) to result in a better model for the eddy viscosity,

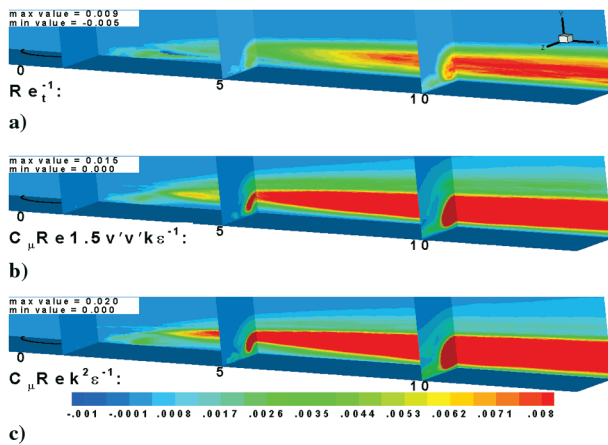


Fig. 11 Eddy viscosity computed using Eq. (11) and modeled eddy viscosity.

particularly near the wall where the overprediction of the eddy viscosity is greatly reduced relative to the  $C_\mu(k^2/\varepsilon)Re$  model.

#### C. Exact $k$ Equation

Figure 12 shows the various terms in the exact  $k$  equation, Eq. (7). For this flow it can be seen that all terms are significant, with the exception of molecular diffusion of  $k$ , which is only important in a very small region very close to the wall. Dissipation appears to be less significant in the CVP, whereas production appears to be more significant there. The dissipation term approximates a negative mirror of the production term in Figs. 12 and 13, with the exception of the wall where the production is zero while dissipation is large. At the wall dissipation is balanced by the diffusion terms  $(\partial/\partial x_2) \times [(1/Re)(\partial k/\partial x_2) - \frac{1}{2}\bar{u}_i' u_i' \bar{u}_2' - \bar{p}' \bar{u}_2']$ , which are the only nonzero terms at the wall. Convective transport of  $k$  is significant, particularly in the CVP, unlike a developed channel flow for which it is theoretically zero. Figures 12e and 12f show the two parts of the turbulent diffusion term, the sum of which are modeled as a diffusion process. Very different distributions are seen between these two terms, which suggests that modeling them as a single diffusion process is inappropriate. This is also seen in Fig. 14 where these terms are of comparable magnitude, whereas for a channel flow the term involving fluctuations in pressure is much smaller. This suggests that models that have been tuned and work well for a channel flow will experience difficulties for a film cooling flow. A rapid change in  $(\partial/\partial x_j)(-\frac{1}{2}\bar{u}_i' u_i' \bar{u}_j')$  (in which the sign changes) can be seen at the top of the jet. This change in sign will be predicted by the gradient of  $k$  (see Fig. 10b), which is used when this term, along with  $(\partial/\partial x_j)(-\bar{p}' \bar{u}_j')$ , is modeled as proportional to the diffusion of  $k$ . However, this same change in sign does not occur in  $(\partial/\partial x_j)(-\bar{p}' \bar{u}_j')$ , which suggests again that this part of the term is not modeled well by being made proportional to the diffusion of  $k$ .

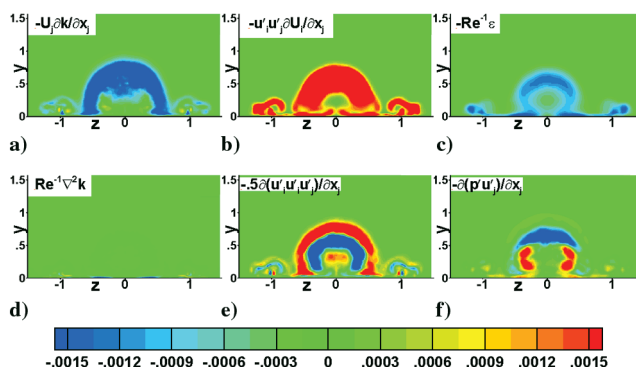


Fig. 12 All terms of exact  $k$  equation [Eq. (7)],  $y-z$  plane at  $y \approx 5d$ .

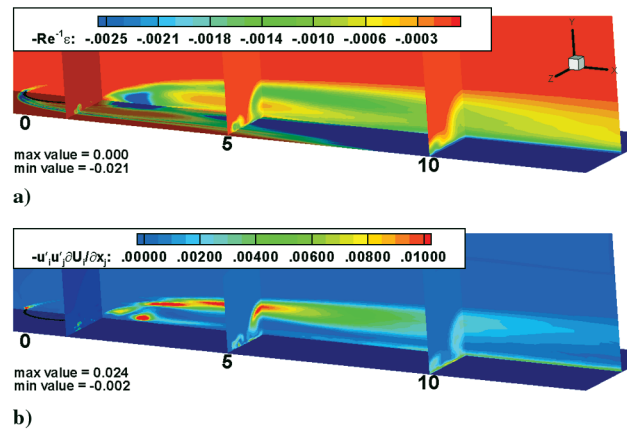


Fig. 13 Three-dimensional view of production and dissipation terms in exact  $k$  equation [Eq. (7)].

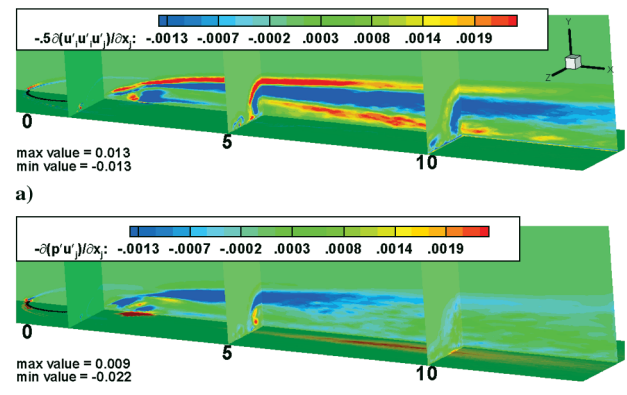


Fig. 14 Three-dimensional view of turbulent diffusion terms in exact  $k$  equation [Eq. (7)].

#### D. Exact $\varepsilon$ Equation

Figure 15 shows the various terms in the exact  $\varepsilon$  equation, Eq. (9). As for the exact  $k$  equation, all terms are significant with the exception of molecular diffusion of  $\varepsilon$ . Production and destruction are approximately negative mirror images of each other near the wall, but away from the wall destruction is positive within the jet. Production is large near the wall, within the horseshoe vortices and within the jet with the exception of a region within the jet where it is small. Convective transport reaches a maximum in the horseshoe vortex and a minimum near the wall in between the CVP and the horseshoe vortex. It is a significant term, unlike a channel flow where it is theoretically zero. Molecular diffusion of  $\varepsilon$  is insignificant except very close to the wall. Figures 15e and 15f show the two parts of the turbulent diffusion term, the sum of which are modeled as a diffusion process. Very different distributions are seen between these two

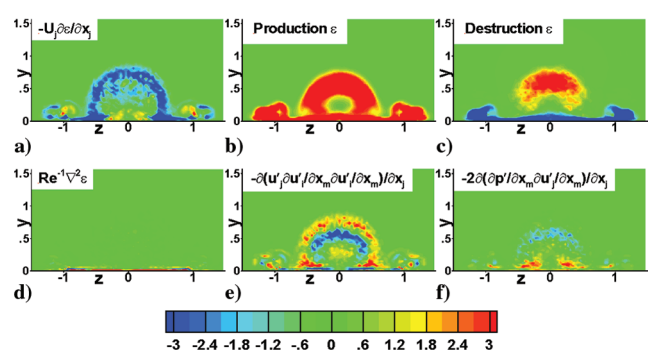


Fig. 15 All terms of exact  $\varepsilon$  equation [Eq. (9)],  $y-z$  plane at  $y \approx 5d$ .

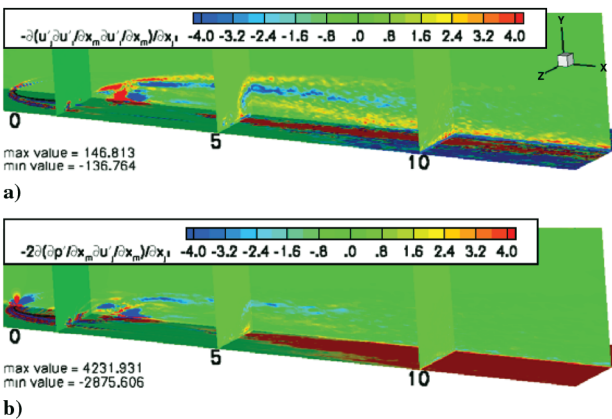


Fig. 16 Three-dimensional view of turbulent diffusion terms in exact  $\varepsilon$  equation [Eq. (9)].

terms, suggesting that modeling them as a single diffusion process is inappropriate. Both parts of the turbulent diffusion of  $\varepsilon$  term are shown in Fig. 16 along the streamwise midplane and three lateral planes. The term involving pressure has extrema nearly two orders of magnitude greater than the other term; however, these extrema are concentrated near the front edge of the jet on the wall (discussed later). In the rest of the flow, the terms are similar in magnitude. This is unlike a channel flow for which the term involving fluctuations in pressure is much smaller. However, they have different distributions, with the term  $(\partial/\partial x_j)(-\bar{u}'_j u'_{i,m} \bar{u}'_{i,m})$  changing sign twice in the vertical direction, whereas  $(\partial/\partial x_j)(-2\bar{p}'_{i,m} u'_{i,m})$  changes sign once. Note that this difference between the term involving pressure and the term that does not is also seen in the exact  $k$  equation.

In Fig. 17a the destruction term is positive in a large region in the jet away from the wall. The production term (see Fig. 17b) is large in the recirculation region and is negative at the wall immediately behind the jet. The extrema in production are concentrated near the front edge of the jet on the wall and are discussed later.

#### E. Modeled $k$ Equation

A comparison of the DNS computed production term  $[-\bar{u}'_i \bar{u}'_j (\partial \bar{u}_i / \partial x_j)]$  with two models,  $2C_\mu(k^2/\varepsilon)ReS_{i,j}S_{i,j}$  and  $2Re_\tau^{-1}S_{i,j}S_{i,j}$ , is given in Fig. 18. Note that the only difference between the two models in Fig. 18 is the eddy viscosity, which is defined to be  $C_\mu(k^2/\varepsilon)Re$  (standard  $k-\varepsilon$  model) or  $Re_\tau^{-1}$  [as obtained from Eq. (11)]. As Eq. (11) finds an eddy viscosity such that it minimizes the error in the approximation of the Reynolds stresses using Eq. (6), it should provide a better approximation of the production term than the standard  $k-\varepsilon$  model, which uses

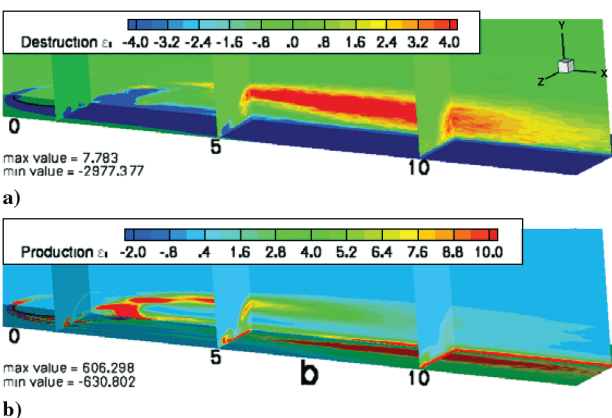


Fig. 17 Three-dimensional view of production and destruction terms in exact  $\varepsilon$  equation [Eq. (9)].

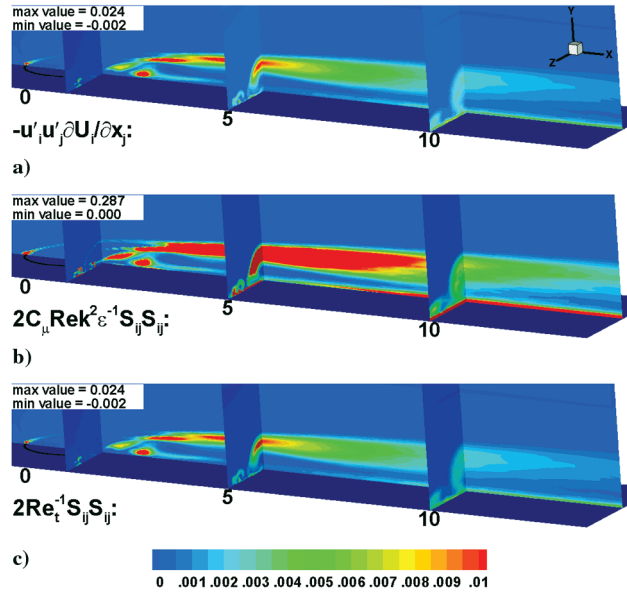


Fig. 18 Production term from exact  $k$  equation [Eq. (7)] vs models.

$C_\mu(k^2/\varepsilon)Re$  to represent the eddy viscosity. The only part of the production term that is modeled is  $\bar{u}'_i \bar{u}'_j$ , and as this is modeled using the Boussinesq gradient approximation, the use of the eddy viscosity found from Eq. (6) results in the best possible model for  $\bar{u}'_i \bar{u}'_j$  when using the Boussinesq gradient approximation. As the errors in the modeled production term are strictly the result of errors in representing the Reynolds stresses, this provides a good measure of the ability of the minimization procedure [Eq. (11)] in combination with the Boussinesq gradient approximation, to represent the Reynolds stresses. It can be seen that using the eddy viscosity computed from Eq. (11) results in almost identically the same value as the DNS computed production term  $[-\bar{u}'_i \bar{u}'_j (\partial \bar{u}_i / \partial x_j)]$ . In contrast, using  $C_\mu(k^2/\varepsilon)Re$  for the eddy viscosity results in an order of magnitude overprediction of the production term, particularly near the blade surface and in the jet region. Nevertheless, the qualitative behavior of the production term is predicted reasonably well using  $C_\mu(k^2/\varepsilon)Re$ . Note that the eddy viscosity computed from Eq. (11) (see Fig. 11) is negative in certain regions, which allows the modeled term  $2Re_\tau^{-1} S_{i,j} S_{i,j}$  to be negative in certain regions, as is the DNS computed production term  $[-\bar{u}'_i \bar{u}'_j (\partial \bar{u}_i / \partial x_j)]$ .

The turbulent diffusion terms  $[(\partial/\partial x_j)(-\frac{1}{2}\bar{u}'_i \bar{u}'_i \bar{u}'_j - \bar{p}' \bar{u}'_j)]$  in the exact  $k$  equation are lumped together and modeled as a single diffusion process in the standard  $k-\varepsilon$  model. Figure 19 compares the DNS computed value of turbulent diffusion  $[(\partial/\partial x_j) \times (-\frac{1}{2}\bar{u}'_i \bar{u}'_i \bar{u}'_j - \bar{p}' \bar{u}'_j)]$  with two models,  $(\partial/\partial x_j)\{[C_\mu(k^2/\varepsilon)Re/\sigma_k] \times (\partial k/\partial x_j)\}$  and  $(\partial/\partial x_j)[(Re_\tau^{-1}/\sigma_k)(\partial k/\partial x_j)]$ , the first of which uses  $C_\mu(k^2/\varepsilon)Re$ , the second  $Re_\tau^{-1}$  [as obtained from Eq. (11)], as the eddy viscosity. The model using an eddy viscosity of  $C_\mu(k^2/\varepsilon)Re$  undershoots the DNS computed value by an order of magnitude. If  $Re_\tau^{-1}$  is used in place of  $C_\mu(k^2/\varepsilon)Re$ , the result is much better. These results demonstrate that the problem with the modeling of this term is with the choice of the eddy viscosity expression. Therefore this term can be modeled well as a diffusion process, if the eddy viscosity is chosen appropriately. The residual (i.e., the imbalance) of all the modeled terms in the modeled  $k$  equation (Fig. 20) illustrates the large errors in the standard  $k-\varepsilon$  model. These errors are particularly large on the wall.

#### F. Modeled $\varepsilon$ Equation

Figure 21 compares the production term of the exact  $\varepsilon$  equation [Eq. (9)] with two models,  $2C_{\varepsilon 1} C_\mu k S_{i,j} S_{i,j} Re$  and  $2C_{\varepsilon 1} \varepsilon k^{-1} Re_\tau^{-1} S_{i,j} S_{i,j}$ , used to represent it. As previously, the only difference between these two models is that, for the eddy viscosity,

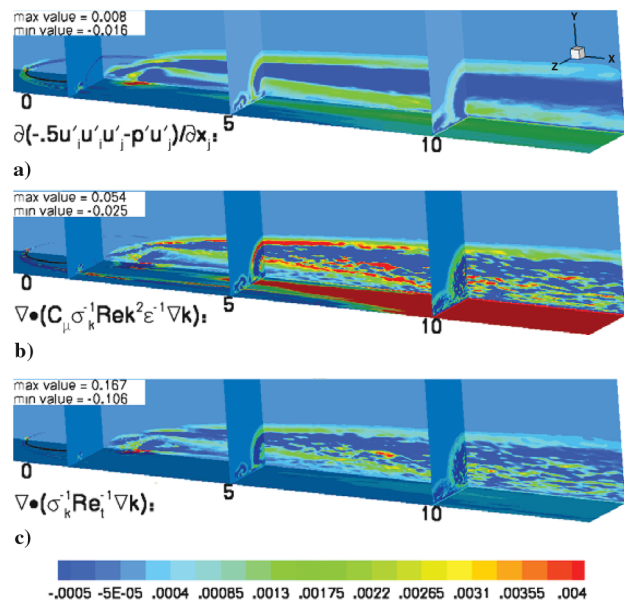


Fig. 19 Turbulent diffusion term from exact  $k$  equation [Eq. (7)] vs models.

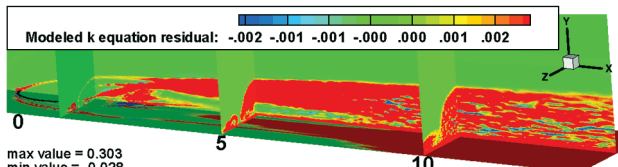


Fig. 20 Three-dimensional view of residual of modeled  $k$  equation [Eq. (8)].

the first uses  $C_\mu(k^2/\varepsilon)Re$  whereas the second uses  $Re_\tau^{-1}$  [as obtained from Eq. (11)]. In Fig. 21, it appears that both models fail to predict the large negative values of the production term, based on the maximum and minimum values reported in the figures. However, these large negative values only appear on the wall at certain locations at the front edge of the jet, where the production term of the exact  $\varepsilon$  equation has large maxima and minima (see Fig. 22a). In the jet region, it can be seen that the model using  $C_\mu(k^2/\varepsilon)Re$  as the eddy

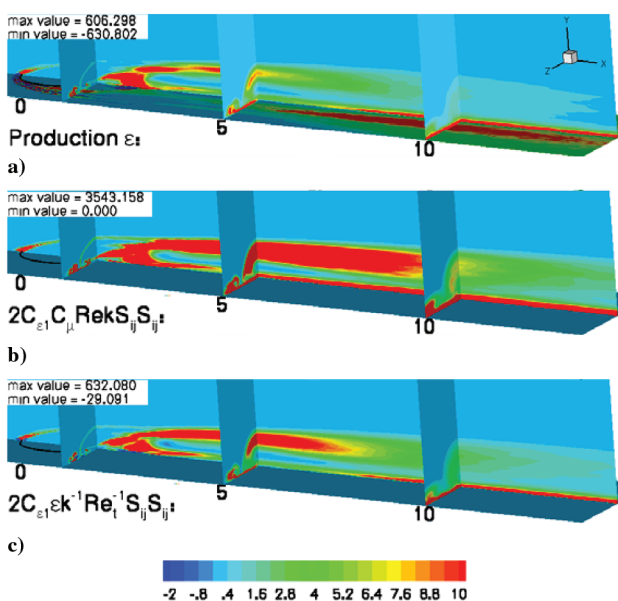


Fig. 21 Three-dimensional view of production term from exact  $\varepsilon$  equation [Eq. (9)] vs modeled term.

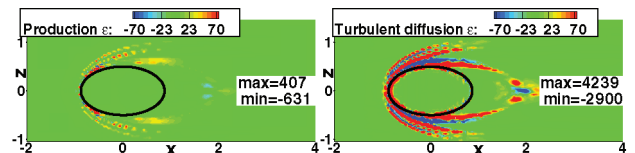


Fig. 22 Production and turbulent diffusion in exact  $\varepsilon$  equation [Eq. (9)] in  $x$ - $z$  plane on the wall.

viscosity greatly overpredicts the production term. The model using  $Re_\tau^{-1}$  [as obtained from Eq. (11)] results in values much closer to that computed from the exact  $\varepsilon$  equation, although it also overpredicts the production in the jet region. Note that both of the models predict a zero value for production on the wall, whereas there is no reason why the actual term in the exact  $\varepsilon$  equation will be zero (see Fig. 21a). For the standard  $k$ - $\varepsilon$  model ( $2C_{\varepsilon 1}C_\mu k S_{i,j} S_{i,j} Re$ ) this zero value on the wall is a result of  $k$  being zero on the wall. For the model using  $Re_\tau^{-1}$  for the eddy viscosity, it is more complicated due to the term  $k^{-1}Re_\tau^{-1}$ , which results in  $0/0$  on the wall. In the present work, this has been defined to be zero. The production term is modeled as a positive term in the standard  $k$ - $\varepsilon$  model; however, on the wall in the recirculation region behind the jet, it assumes large negative values. Note that negative values are allowed in the model that uses  $Re_\tau^{-1}$ , as  $Re_\tau^{-1}$  may be negative and indeed is so in part of the recirculation region.

As the destruction term in the exact  $\varepsilon$  equation is believed to be primarily negative, the standard  $k$ - $\varepsilon$  model represents this term by an expression  $[-C_{\varepsilon 2}(\varepsilon^2/kRe)]$  that is always less than or equal to zero. Figure 23 shows that this term, as computed from the exact  $\varepsilon$  equation, has very large negative values next to and on the wall, but that it is positive (although small) in the jet region away from the wall. The model underpredicts the destruction term in the recirculation region behind the jet. The destruction term, as computed from both the exact  $\varepsilon$  equation and the model, shows significant negative values within the horseshoe vortex at  $x \approx 5d$ , although only in the model does this persist downstream. Note that as a result of division by  $k$  the model is ill-behaved in parts of the flow, such as the freestream where  $k$  approaches zero, near the wall where  $k$  also approaches zero, and at the wall where  $k$  is zero.

Figure 24 compares the turbulent diffusion term of the exact  $\varepsilon$  equation with two models,  $(\partial/\partial x_j)[(C_\mu Re/\sigma_\varepsilon)(k^2/\varepsilon)(\partial\varepsilon/\partial x_j)]$  and  $(\partial/\partial x_j)[(Re_\tau^{-1}/\sigma_\varepsilon)(\partial\varepsilon/\partial x_j)]$ , used to represent it. Again, the only difference between these two models is that, for the eddy viscosity, the first uses  $C_\mu(k^2/\varepsilon)Re$  whereas the second uses  $Re_\tau^{-1}$  [as obtained from Eq. (11)]. As is the case for the production term of the exact  $\varepsilon$  equation, the maximum and minimum values of the turbulent diffusion term from the exact  $\varepsilon$  equation occur on the wall at certain locations at the front edge of the jet (see Fig. 22b). In the jet region, the model using  $C_\mu(k^2/\varepsilon)Re$  as the eddy viscosity greatly under- and overpredicts turbulent diffusion, whereas the model using  $Re_\tau^{-1}$  is a significant improvement. This overprediction by the model using  $C_\mu(k^2/\varepsilon)Re$  is also seen in the horseshoe vortex system. However,

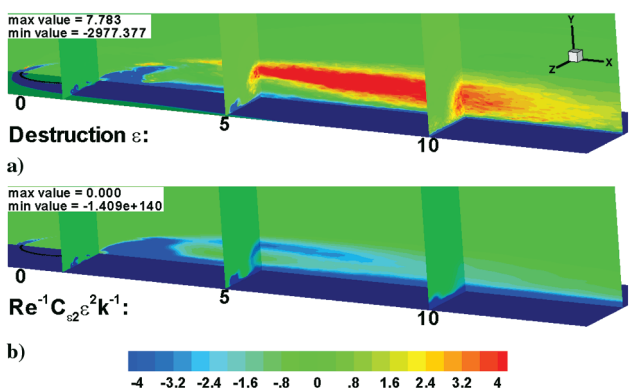


Fig. 23 Three-dimensional view of destruction term from exact  $\varepsilon$  equation [Eq. (9)] vs model.

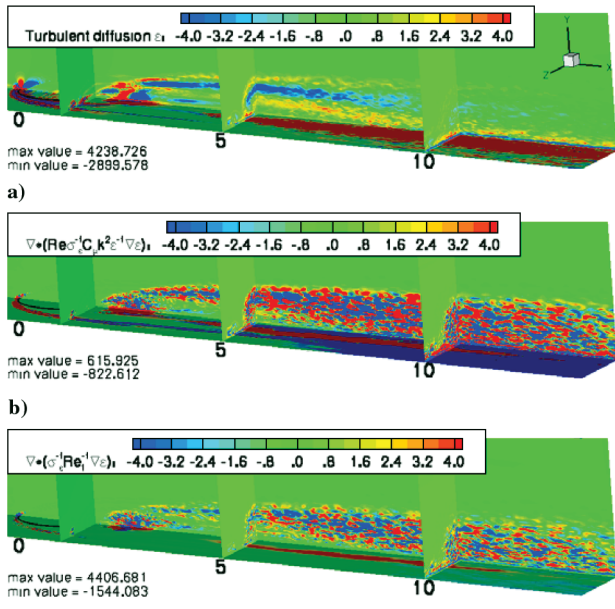


Fig. 24 Turbulent diffusion term from exact  $\varepsilon$  equation [Eq. (9)] vs models.

both models qualitatively predict the behavior of this term correctly, as both predict a positive region at the outer edge of the jet, a negative region inside this, and another positive region inside the negative region.

#### G. Damping Function

A serious problem with the standard  $k-\varepsilon$  model is that it overpredicts the eddy viscosity (see Fig. 11). This error can be reduced by the use of what is termed a damping function, designed to reduce or damp the eddy viscosity. The damping function ( $f_\mu^{\text{dns}}$ ) used in the present work is intended for use as in Eq. (12).

$$-\overline{u'_i u'_j} = f_\mu^{\text{dns}} C_\mu \frac{k^2}{\varepsilon} Re 2 S_{i,j} - \frac{2}{3} k \delta_{i,j} \quad (12)$$

Equating Eq. (6) with Eq. (12) yields a definition of the damping function [Eq. (13)] where all terms on the right-hand side are determined from DNS data.

$$f_\mu^{\text{dns}} = \frac{Re_\tau^{-1}}{C_\mu (k^2/\varepsilon) Re} \quad (13)$$

From the DNS data  $f_\mu^{\text{dns}}$  is defined at every discrete point in the spatial domain. For practical use, however, it must be a simple expression of variables available in turbulence models. There are various damping functions in the literature [17]; generally, if designed using DNS data, they have been obtained from simple flows such as flow in a channel or a boundary layer in which two directions are homogeneous. The damping function is commonly made a function of a nondimensional distance [ $y^+ = y \sqrt{(\rho/\mu)(\partial u/\partial y)}$ ] from the wall. The damping function proposed by Rodi and Mansour [17] was obtained by fitting a function dependent on  $y^+$  to DNS data for a channel flow. However, the use of this nondimensional distance to construct a damping function for a highly three-dimensional flow, with no homogeneous directions, is problematic. Figure 25 shows that plotting  $f_\mu^{\text{dns}}$  vs  $y^+$  does not collapse well, whereas it does so if plotted against  $y$ . The reason for this is that, unlike in a channel flow, the wall shear is not a constant but instead varies across the wall in both directions; indeed there are places, such as in the recirculation region behind the jet, where the wall shear may be zero. This makes it impossible to parameterize with  $y^+ = y \sqrt{(\rho/\mu)(\partial u/\partial y)}$ .

The damping function does correlate well with the wall normal turbulent fluctuations normalized by the turbulent kinetic energy

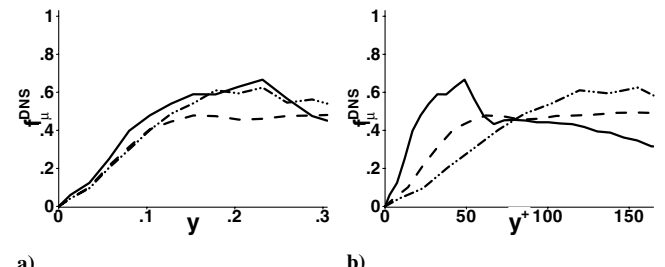


Fig. 25 Damping function at  $z = 0$  at different  $x$  locations.

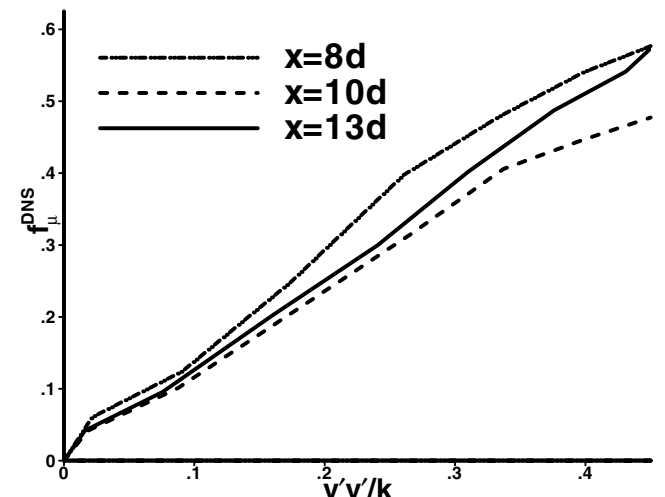


Fig. 26 Damping function as a function of  $v'v'/k$  at  $z = 0d$  at different  $x$  locations.

$v'v'/k$ . The behavior of the damping function is that it increases approximately linearly in  $y$  in the wall normal direction from zero at the wall to  $\sim \frac{1}{2}$  in the freestream. Plotting the damping function vs  $v'v'/k$  shows a linear relationship in a certain region. However, the damping function is not a unique one to one function of  $v'v'/k$ , so starting from zero at the wall or zero in the freestream there are two possible directions to take. The first, which quickly leads to a peak in the damping function, is the same peak that occurs in the freestream; therefore, this branch is the one starting in the freestream. The second (which increases approximately linearly from zero and asymptotes to  $\sim \frac{1}{2}$ ) is the one starting at the wall and shown in Fig. 26. From this behavior a simple equation can be written which approximates the dependence of the damping function on the wall normal turbulent fluctuations [Eq. (14)].

$$f_\mu^{\text{dns}} \left( \frac{v'v'}{k} \right) = \begin{cases} \frac{0.5}{0.375} \frac{v'v'}{k} & \text{for } 0 \leq \frac{v'v'}{k} \leq 0.375 \\ 0.5 & \text{for } \frac{v'v'}{k} > 0.375 \end{cases} \quad (14)$$

The purpose of this equation is to damp the eddy viscosity near the wall using the wall normal turbulent fluctuations (which are very sensitive to the presence of a wall) as a measure of the distance from the wall. This idea is not new; the  $v^2 f - k \varepsilon$  model of Durbin [25,26] is based on this observation. Figure 27 shows the improvement obtained from the new damping function as the overprediction of the eddy viscosity is greatly reduced whereas the correct qualitative behavior of the eddy viscosity is maintained.

Whereas the wall normal turbulent fluctuations correlate well with the damping function, they are not available in a two-equation turbulent model such as the  $k-\varepsilon$  model. Therefore Eq. (14) cannot be used with such turbulence models. A damping function for two-equation turbulent models must be based on the variables available in such models. If  $\mu/\sqrt{k}\rho$  is used as a characteristic length (based on the equilibrium assumption), a different nondimensional distance ( $y_k^+$ ) from the wall can be defined which correlates well with the

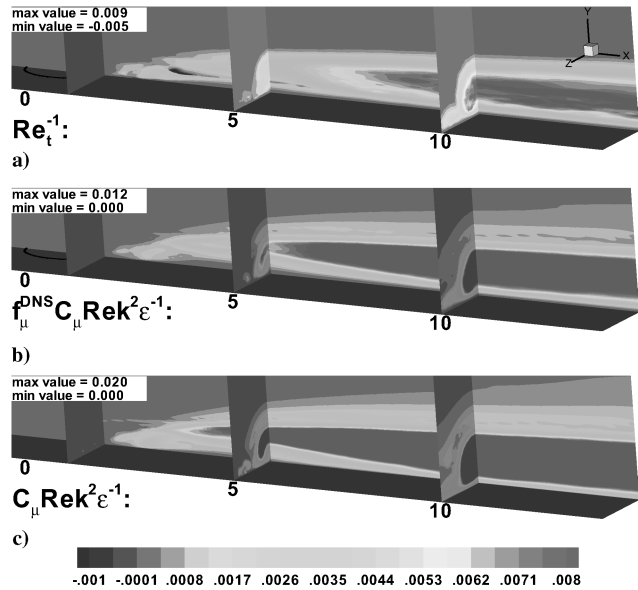


Fig. 27 a) Eddy viscosity computed from Eq. (11), b) modeled eddy viscosity with new damping function Eq. (14), c) modeled eddy viscosity.

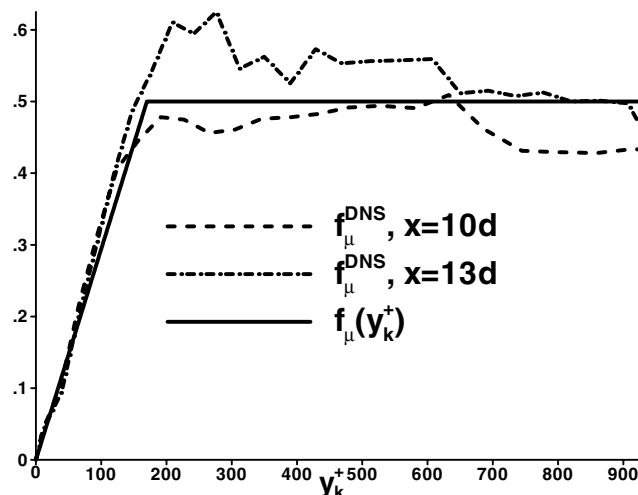


Fig. 28 Damping function at  $z = 0d$ ,  $0 \leq y \leq 0.9$ .

damping function. With the nondimensionalization used in the present work, this results in  $y_k^+ = y\sqrt{k}Re$ . When the damping function is plotted (Fig. 28) against  $y_k^+$ , similar behavior is found as when plotted against  $\bar{v}'\bar{v}'/k$ . Equation (15) gives a simple expression which captures the behavior of the damping function as a function of  $y_k^+$  well (see Fig. 28).

$$f_\mu^{\text{dns}}(y_k^+) = \begin{cases} \frac{0.5}{170}y_k^+ & \text{for } 0 \leq y_k^+ \leq 170 \\ 0.5 & \text{for } y_k^+ > 170 \end{cases} \quad (15)$$

Figure 29 shows the result of using Eq. (15); it is similar to the improvement obtained from the damping function based on  $\bar{v}'\bar{v}'/k$  [Eq. (14)] but may be used with two-equation turbulence models.

## IX. Conclusions

Using direct numerical simulation, all terms in the exact  $k$  and  $\epsilon$  equations have been computed and compared with the standard  $k-\epsilon$  model for a film cooling jet flow. The effect of the grid spacing on the results using three different grids has been studied and along with the spatial energy spectrum shows that the important turbulent scales have been resolved. The residuals of the exact  $k$  and  $\epsilon$  equations decrease as the grid spacing decreases, indicating that the terms in these equations have been properly computed.

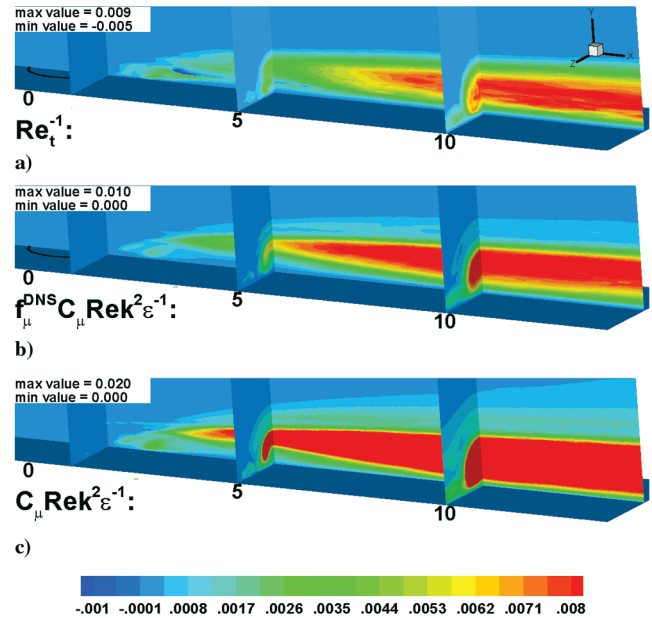


Fig. 29 a) Eddy viscosity computed from Eq. (11), b) modeled eddy viscosity with new damping function Eq. (15), c) modeled eddy viscosity.

Unlike a channel flow, the terms in the exact  $k$  and  $\epsilon$  equations that contain correlations involving pressure have been shown to be significant for a film cooling jet. In addition, the correlations involving pressure have been shown to behave differently than the correlations involving just the velocity, contrary to what is typically assumed. This is of interest as turbulence models commonly model these two terms as a single diffusion process.

The eddy viscosity concept has been tested extensively by comparing the terms in the exact  $k$  and  $\epsilon$  equations computed from DNS to the standard  $k$  and  $\epsilon$  models for the terms and also to the same standard  $k$  and  $\epsilon$  models using an eddy viscosity obtained from DNS. The greatest weakness in the standard  $k-\epsilon$  model has been shown to be the choice of the eddy viscosity. If the eddy viscosity is chosen by a method that applies a minimization procedure to the DNS data, the various models for the terms in the exact  $k$  and  $\epsilon$  equations represent the terms relatively well. Therefore the challenge is to improve the model for the eddy viscosity. A step is made in this direction by two proposed new damping functions. The first damping function is based on the wall normal turbulent fluctuations and is shown to greatly reduce the overprediction of the eddy viscosity in the standard  $k-\epsilon$  model. However, this damping function based on the wall normal turbulent fluctuations cannot be used with two-equation turbulence models such as the standard  $k-\epsilon$  model. To alleviate this problem, a second new damping function is proposed which can be used by two-equation turbulence models. This damping function is based on a nondimensional distance from the wall and is shown to greatly improve the computation of the eddy viscosity in the standard  $k-\epsilon$  model.

## Acknowledgments

This work was supported by the Office of Naval Research and the Center for Computation and Technology at Louisiana State University. The simulations were run on workstations at the Center for Computation and Technology at Louisiana State University, the Linux Xeon cluster SuperMike and Helix at Louisiana State University, the IBM machine Casper at Louisiana State University, and an IBM SP4 at the Arctic Region Supercomputing Center.

## References

- [1] Hoda, A., and Acharya, S., "Predictions of a Film Coolant Jet in Crossflow With Different Turbulence Models," *Journal of Turbomachinery*, Vol. 122, No. 3, 2000, pp. 558–569.

- [2] Wilcox, D., *Turbulence Modeling for CFD*, Birmingham Press, Inc., San Diego, CA, 1993.
- [3] Ajersch, P., Zhou, J.-M., Ketler, S., Salcudean, M., and Gartshore, I. S., "Multiple Jets in a Crossflow: Detailed Measurements and Numerical Simulations," ASME Paper 95-GT-9, 1995.
- [4] He, P., Salcudean, M., and Gartshore, I. S., "Computations of Film Cooling for the Leading Edge Region of a Turbine Blade Model," ASME Paper 95-GT-20, 1995.
- [5] Berhe, M. K., and Patankar, S. V., "A Numerical Study of Discrete-Hole Film Cooling," ASME Paper 96-WA-HT-8, 1996.
- [6] Berhe, M. K., and Patankar, S. V., "Computation of Discrete-Hole Film Cooling: A Hydrodynamic Study," ASME Paper 97-GT-80, 1997.
- [7] Harrington, M. K., McWaters, M. A., Bogard, D. G., Lemmon, C. A., and Thole, K. A., "Full-Coverage Film Cooling with Short Normal Injection Holes," ASME Paper 2001-GT-0130, 2001.
- [8] Radomsky, R. W., and Thole, K. A., "Measurements and Predictions of a Highly Turbulent Flowfield in a Turbine Vane Passage," *Journal of Fluids Engineering*, Vol. 122, No. 1, 2000, pp. 666-676.
- [9] Medic, G., and Durbin, P., "Toward Improved Prediction of Heat Transfer on Turbine Blades," *Journal of Turbomachinery*, Vol. 124, No. 2, 2002, pp. 187-192.
- [10] Medic, G., and Durbin, P., "Toward Improved Film Cooling Prediction," *Journal of Turbomachinery*, Vol. 124, No. 2, 2002, pp. 193-199.
- [11] Hahn, S., and Choi, H., "Unsteady Simulation of Jets in Crossflow," *Journal of Computational Physics*, Vol. 134, No. 2, 1997, pp. 342-356.
- [12] Muldoon, F., and Acharya, S., "Numerical Investigation of the Dynamical Behavior of a Row of Square Jets in Crossflow over a Surface," ASME Paper 98-GT-019, 1999.
- [13] Tyagi, M., and Acharya, S., "Large Eddy Simulations of Rectangular Jets in Crossflow: Effect of Hole Aspect Ratio," *Recent Advances in DNS and LES, Second AFSOR Conference on DNS/LES*, edited by D. Knigh and L. Sakell, Springer-Verlag, New York, 1999, pp. 431-442.
- [14] Tyagi, M., and Acharya, S., "Large Eddy Simulations of Jets in Crossflow: 2, Effect of Freestream Turbulence Length Scale Effects," *Journal of Energy, Heat and Mass Transfer*, Vol. 25, No. 1, 2003, pp. 95-116.
- [15] Tyagi, M., and Acharya, S., "Large Eddy Simulations of Jets in Crossflow: Freestream Turbulence Intensity Effects," ASME-FEDSM Paper 99-7799, 1999.
- [16] Mansour, N. N., Kim, J., and Moin, P., "Reynolds Stress and Dissipation-Rate Budgets in a Turbulent Channel Flow," *Journal of Fluid Mechanics*, Vol. 194, No. 2, 1988, pp. 15-44.
- [17] Rodi, W., and Mansour, N. N., "Low Reynolds Number  $k-e$  Modeling with the Aid of Direct Simulation Data," *Journal of Fluid Mechanics*, Vol. 250, May 1993, pp. 509-529.
- [18] Muldoon, F., "Numerical Methods for the Unsteady Incompressible Navier-Stokes Equations and Their Application to the Direct Numerical Simulation of Turbulent Flows," Ph.D. Thesis, Louisiana State Univ., Baton Rouge, LA, 2004.
- [19] Launder, B. E., and Spalding, D. B., "The Numerical Computation of Turbulent Flows," *Computer Methods in Applied Mechanics and Engineering*, Vol. 3, 1974, pp. 269-275.
- [20] Kaszeta, R. W., "Measurements in Film Cooling Flows with Lateral Injection," M.S. Thesis, Univ. of Minnesota, 1998.
- [21] Kolmogoroff, A. N., "The Local Structure of Turbulence in Incompressible Viscous Fluid for Very Large Reynolds Number," *Comptes Rendus de l'Academie des Sciences de l'URSS / Doklady Akademii Nauk SSSR*, Vol. 30, 1941, pp. 301-305.
- [22] Oran, E. S., and Boris, J. P., *Numerical Simulation of Reactive Flow*, Press Syndicate of the University of Cambridge, Cambridge, England, U.K., 2001.
- [23] Voke, P. R., Yang, Z., and Gao, S., "Extracting Reynolds-Stress and Dissipation Budgets from Finite Volume Simulations of Turbulence," *International Journal of Computational Fluid Dynamics*, Vol. 8, 1997, pp. 115-128.
- [24] Fric, T. F., and Roshko, A., "Vortical Structure in the Wake of a Transverse Jet," *Journal of Fluid Mechanics*, Vol. 279, Nov. 1994, pp. 1-47.
- [25] Durbin, P. A., "Near-Wall Turbulence Closure Modeling Without 'Damping Functions,'" *Theoretical and Computational Fluid Dynamics*, Vol. 3, No. 1, 1991, pp. 1-13.
- [26] Durbin, P. A., "Separated Flow Computations with the K-e-Vv Model," *AIAA Journal*, Vol. 33, No. 4, 1995, pp. 659-664.

P. Givi  
Associate Editor